Combustion and Flame 252 (2023) 112747

Contents lists available at ScienceDirect

Combustion and Flame

journal homepage: www.elsevier.com/locate/combustflame

Imaging the combustion characteristics of Al, B, and Ti composites

Yujie Wang, Erik Hagen, Prithwish Biswas, Haiyang Wang, Michael R. Zachariah*

University of California, Riverside, CA 92521, United States

ARTICLE INFO

Article history:
Received 3 December 2022
Revised 17 March 2023
Accepted 17 March 2023
Available online 29 March 2023

Keywords:
Combustion
Aluminum
Boron
Titanium
Imaging
Pyrometry

ABSTRACT

In this study, we prepare 90 wt% loading composites of Al, B, and Ti with $KClO_4$ by 3D printing and study their combustion characteristics with high-speed videography and pyrometry. Combustion characteristics are found to be strongly dependent on the fuel type. For Al, Al droplets with Al_2O_3 caps form and coalesce before departing the burning surface, while for B and Ti, fractal-shaped agglomerates form. Temperatures of the burning particles (droplet/agglomerates) are determined with color imaging-pyrometry. The combustion characteristics are attributed to the physical properties, e.g. melting and boiling points, of these fuels and their corresponding oxides. We observe particles residing and burning on the propellant surface for times on the order of ~1–5 ms. This is significantly lower than the theoretical particle burn time, suggesting particles undergo incomplete combustion on the burning surface, consistent with the experimental observation that particles continue to burn after departing the surface. The estimated particle downstream burning distance is significantly larger than the observed luminous zone, implying it does not represent the complete flame zone. Since Al undergoes vapor phase combustion while B and Ti combust in the condense phase, burn rate of Al should be drastically higher than B and Ti, However, the differences are not as significant as expected. This is attributed to the formation of much larger droplets for Al that results in dramatically longer particle burn times.

1. Introduction

Energetic nanocomposites, such as nanothermites typically consist of nanoscale fuels and oxidizers, offer higher energy release rates compared to their micron counterparts due to significantly increased interfacial area and reduced diffusion distance between fuel and oxidizer [1–3]. Nevertheless the enhanced combustion rates are not as high as they should be based on simple theoretical arguments. One contributing factor is the loss of nanostructure during a reaction, which may be responsible for the lower than expected energy release rate [4–8]. The loss of nanostructure from reactive sintering has a significant impact on the combustion behavior of the composite [7]. Nanoscale aluminum, boron, and titanium are attractive in nanothermites based on their potential as high energy density fuels and possess very different physical properties such as metal and metal oxide melting points, which can impact sintering rates [9–12]. Aluminum has been used as the primary fuel in solid rocket propellant and other propulsive systems due to its ready availability and high enthalpy [13–15]. Boron has very high gravimetric and volumetric energy content and titanium is a viable alternative fuel source [11,16–18]. Therefore probing and understanding the combustion dynamics of these nanoscale fuels are essential for their practical application.

Previous studies have demonstrated that imaging techniques are particularly useful in probing spatial and temporal combustion dynamics [19–21]. Studies investigating aluminum particle combustion have utilized imaging techniques coupled with holography and pyrometry for quantifying position, size, and velocity of aluminum particles as well as estimating particle temperatures [22,23]. Although titanium and boron combustion has been investigated with videography and pyrometry [18,24–26], these studies are far less prevalent as compared to aluminum, and a systematic study focusing on combustion behavior differences among different metal fuels is still lacking.

In this paper, we prepare free-standing $KClO_4$/nanoscale Al, B, and Ti composites at 90% loading by 3D printing, and investigate their combustion characteristics systematically. $KClO_4$ is used as the oxidizer since its decomposition products, O_2 and KCl (boiling point of 1412 °C) [27,28], are gaseous at the temperature of interest, thus presumably there is little condensed-phase residue interacting with fuel agglomerates during combustion. High-speed (μs) videos at high resolution (μm) are obtained for visualizing the combustion processes and physical properties of the as-formed agglomerates in-operando. Color imaging pyrometry is utilized to estimate the temperature profile of the reacting zone and provide information about the particle combustion of these met-

* Corresponding author.
E-mail address: mrz@engr.ucr.edu (M.R. Zachariah).

https://doi.org/10.1016/j.combustflame.2023.112747
0010-2180/

als. Scanning Electron Microscopy (SEM) with energy-dispersive spectrometry (EDS) is employed to analyze the post-combustion product and provide insight into combustion process. Burn rate of these composites are measured and relative energy release rate are calculated.

2. Materials and methods

2.1. Materials

Aluminum nanoparticles (Al NPs, ~50 nm, 67 wt% active) were obtained from Argonide Corporation. Titanium nanoparticles (Ti NPs, ~50 nm, 70 wt% active) and boron nanoparticles (B NPs, ~100 nm, 85 wt% active) were purchased from US Research Nanomaterials. The active content of these fuels was determined with thermogravimetry and differential scanning calorimetry (TGA–DSC) using a Netsch STA449 F3 Jupiter thermal analyzer. Potassium perchlorate ($KClO_4$, 99%) was purchased from Alfa Aesar. Polyvinylidene Fluoride (PVDF, average molecular weight: ~534,000) was purchased from Sigma-Aldrich and METHOCEL^{TM} F4M Hydroxypropyl Methylcellulose (HPMC) was obtained from Dow Chemical Company. *N,N*-Dimethylformamide (DMF, 99.8%) was purchased from Fisher Scientific and used as a solvent to dissolve the above polymers as well as $KClO_4$.

2.2. Preparation of ink and direct ink writing of 90 wt% loading M/$KClO_4$ composites

The details on ink preparation and printing with 90 wt% nanoparticle loading composites can be found in our previous study [29]. Generally, the inks were prepared by firstly dissolving 4 wt% of PVDF and 6 wt% of HPMC or 10 wt% PPC in DMF (all composites use PVDF/HPMC as binders unless otherwise noted). The effect of binder (4 wt% of PVDF and 6 wt% of HPMC) on combustion of the agglomerates is believed to be insignificant due to the low content, low gas generation, and minimal chemical reactions between the fuels and the decomposition product of the polymers [57]. $KClO_4$ was then dissolved in this solution and fuel nanoparticles were added to the obtained solution. The mixture was then ultrasonicated for 30 min and magnetically stirred overnight. The amount of fuel and $KClO_4$ was determined with the following equations to prescribe the stoichiometric ratio.

$$8Al + 3KClO_4 = 4Al_2O_3 + 3KCl \quad (1)$$

$$8B + 3KClO_4 = 4B_2O_3 + 3KCl \quad (2)$$

$$2Ti + KClO_4 = 2TiO_2 + KCl \quad (3)$$

For printing, an ink was extruded through an 18-gauge nozzle and directly written in a pre-designed pattern on a preheated (~75 °C) glass substrate. During printing, we ensured that every layer was dry before the deposition of the next layer. After printing, the obtained films were heated at ~75 °C for 30 min to remove the remaining solvent. Then the films were cut into ~2 cm long sticks for combustion characterizations.

2.3. SEM/EDS

The morphology and composition of the 3D-printed samples and combustion residues were characterized by scanning electron microscope (SEM, Thermo-Fisher Scientific NNS450) coupled with energy dispersive X-ray spectroscopy (EDS). SEM images of the as-received fuel nanoparticles and cross section of the printed sticks are displayed in Figs. S1 and S2, respectively. The post-combustion product was collected by placing a piece of carbon tape ~1.5 cm away from a printed composite before combustion tests. For Al-$KClO_4$, the larger particles did not attach on the tape probably because of the deposition of KCl and aluminum oxide nanoparticles (as shown in Fig. S3). To resolve this issue and visualize larger agglomerates in SEM, post-combustion product of Al-$KClO_4$ was collected on glass at the same distance from the composite (~1.5 cm), then the product was washed with water briefly to dissolve KCl nanoparticles. To minimize oxidation of the particles from water, the washing process was performed by adding water to the post-combustion product and followed by immediate vortexing for ~20 s. Then the suspension was centrifuged immediately, and precipitate was collected and dried under vacuum in a desiccator before SEM.

2.4. Microscopic and macroscopic imaging

The details of the imaging process can be found in previous publications from our group [30]. Generally, two imaging systems were used for capturing the combustion process of the composites. One of them was the microscopic imaging system with high-speed camera (Vision Research Phantom VEO710L) coupled with Infinity Photo-Optical Model K2 DistaMax, and the other one was the macroscopic imaging system with high-speed camera (Phantom V12.1). Printed sticks (~2 cm long) were mounted on a stage inside a chamber filled with argon that was placed between the two imaging systems and settings were adjusted so that the surfaces of the sticks were in focus in two imaging systems. The sticks were then ignited with a Joule-heated nichrome wire. The burning process was recorded at a sample rate of 24,000 frame/s (512 × 512 pixels, 1.7 μm/pixel) with a microscopic imaging system and 10,000 frame/s with the macroscopic imaging system.

Size measurement was performed with ImageJ. Only particles that were about to depart from the burning surface or already departed were measured. For B-$KClO_4$ and Ti-$KClO_4$, agglomerates we observed, so an area equivalent diameter is reported. To obtain reasonable statistics at least 120 particles were measured for each composite.

2.5. Three-color imaging pyrometry

Details about three-color imaging pyrometry can be found in our previous studies [1,31,32]. Briefly, channel intensities of three colors (red, green, and blue) from the Bayer filter and their ratios were used for estimating the temperature of the sample with a custom MATLAB routine assuming graybody emission behavior of the sample. Calibration factors were obtained by the response to a blackbody source (Mikron M390). Temperature uncertainty was estimated to be nominally 200–300 K [31,33].

It is worth noting that we use the entire spectral range for the temperature measurement, the issues with which as McNesby et al. pointed out [56], is the possibility of atomic/molecular interference which leads to error in temperature calculation. We have estimated the error being less than 300 K based on black body calibration and wire emission for this study. When the error exceeds this threshold, the data is removed. For this study interference from atomic/molecular emission BO_2 has characteristic green emission that results in error in temperature calculation. To circumvent this problem, two-color pyrometry is used for measuring the agglomerate temperature of B-$KClO_4$, the details of which can be found in 2.6.

2.6. Two-color imaging pyrometry

For the sample of B-$KClO_4$, imaging data was also processed as two-color pyrometry similarly to the three-color process, using a short pass filter (Edmunds Optics, 625 nm 50 mm diameter, OD 4.0 Shortpass Filter #84-724) placed between the camera and the sample to cut-off wavelengths above 625 nm. The theoretical curves were generated using Planck's law and the response spectrum of the CMOS sensor of the camera after removing wavelengths above 625 nm from the response spectrum. These curves were then fitted to a polynomial. The usage of the short pass filter resulted in a different calibration curve compared to the previous calibration result without the filter, therefore calibration was performed with a short pass filter. Calibration data obtained with a black body source (Mikron M390) at known temperatures were compared with the theoretical curves and was fit to a linear correction function with the corrected estimated error being 2–4%. A custom MATLAB script demosaiced the videos and used the polynomial fit from the theoretical curves and linear correction function to estimate the temperature of the burning particles. Two-color (red and blue) pyrometry was used by neglecting the green channel when analyzing the B-$KClO_4$ composite, as the green molecular emission from BO_2 corrupts the temperature estimation.

2.7. CHEETAH calculation

CHEETAH was performed with constant pressure (1 atm) where only the fuel (including native oxide) and the oxidizer of the composites were considered.

3. Results and discussion

3.1. Combustion behavior at the microscopic scale

High-speed microscopic video enables direct observation of events near the flame front and adds insight into the combustion behavior of a thermite reaction. Figure 1 displays the representative snapshots taken from the high-speed microscopic videos for different composites. (The microscopic videos are shown as Videos S1, S2, and S3, while macroscopic videos are shown as Video S4). All the three composites show cone-shaped flame front that is attributed to the porosity difference arising from printing, where the edge of the stick has a higher solvent evaporation rate that results in a higher porosity.

As shown in Fig. 1(a) and Video S1 in supplementary materials, molten droplets form on the burning surface of Al-$KClO_4$. Prior to departing from the burning surface, the moving droplets coalesce into larger droplets with sizes typically below 150 μm (Fig. 2). The molten droplets, particularly those leaving the burning surface, are surrounded by smoke which are presumably dispersed aluminum oxide particles nucleated from the oxidation of aluminum vapor [20,22]. The dark lobes on the molten droplets are Al_2O_3 caps, which may form from three sources: (1) phase separation of the native oxide shell (33 wt%) of Al nanoparticles along sintering/coalescence, (2) condensation of oxide smoke, and (3) Al droplet oxidation (mostly happens before departing from the burning surface) [20,34,35]. For the latter, oxygen penetrates into an Al droplet and Al-O solution forms, which then phase separates into liquid Al and Al_2O_3 when the dissolved oxygen reaches the solubility limit [20]. Following phase separation, the oxide retracts into a distinct cap through surface tension forces [35]. Rotation is observed on most of the departed droplets, although the rotation frequency varies significantly, for example ~4800 Hz vs ~400 Hz as shown in Figs. S4 and S5 and is due to asymmetric burning of the particle, leading to asymmetric gas generation [23,34,36]. Bubbling and bursting of droplets are also observed, as shown in Fig. S6.

B-$KClO_4$ and Ti-$KClO_4$ burn similarly to each other but dramatically differently as compared to Al-$KClO_4$. As illustrated in Fig. 1(b) and (c) as well as Videos S2 and S3, burning particles agglomerate and form fractal-shaped structures before leaving the burning surface. The size distribution of the burning particles is displayed in Fig. 2. Some agglomerates melt and shrink to be spheres, as shown in Figs. S7 and S8, and the agglomerates from Ti-$KClO_4$ have a higher tendency to become spheres than B-$KClO_4$, the reasons for which will be discussed in Section 3.3. Around the burning surface of B-$KClO_4$, a characteristic green color arising from the emission of BO_2 is observed [37,38]. As for Ti-$KClO_4$, emission from TiO is responsible for the red-orange glow around the burning surface [39].

SEM images and corresponding size distributions of the as-received nanoparticles show that the size is generally below 150 nm for Al, 600 nm for B, and 200 nm for Ti (Fig. S1). Size comparison between these initial fuel nanoparticles and the microdroplets/particles formed during combustion reveals extensive sintering/agglomeration of these fuels, as the size increases ~800 times for Al, ~150 times for B, and ~550 times for Ti.

3.2. Temperature measurement from imaging-pyrometry

Three-color (RGB) imaging-pyrometry is employed for temperature estimation of Al-$KClO_4$. Smoke present around Al/Al_2O_3 droplets can bias droplet temperature estimation when the smoke is optically thick. To evaluate the effect of the smoke on temperature estimation (details can be found in Section S3), the optical thickness is estimated based on Eq. (S1), and demonstrates that the smoke is optically thin (optical thickness less than 0.1

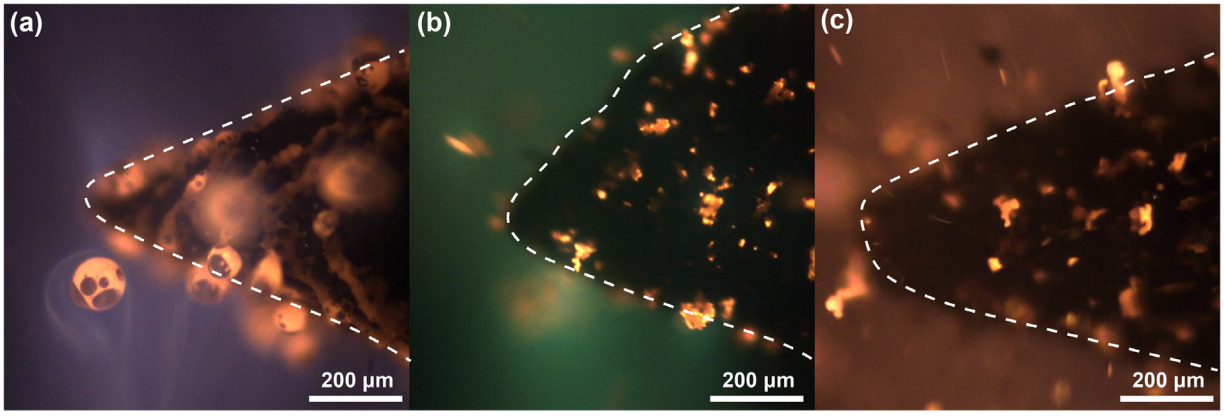

Fig. 1. Images from high-speed microscopy videos for (a) Al-$KClO_4$, (b) B-$KClO_4$, and (c) Ti-$KClO_4$. The dashed lines represent boundaries of the burning surfaces.

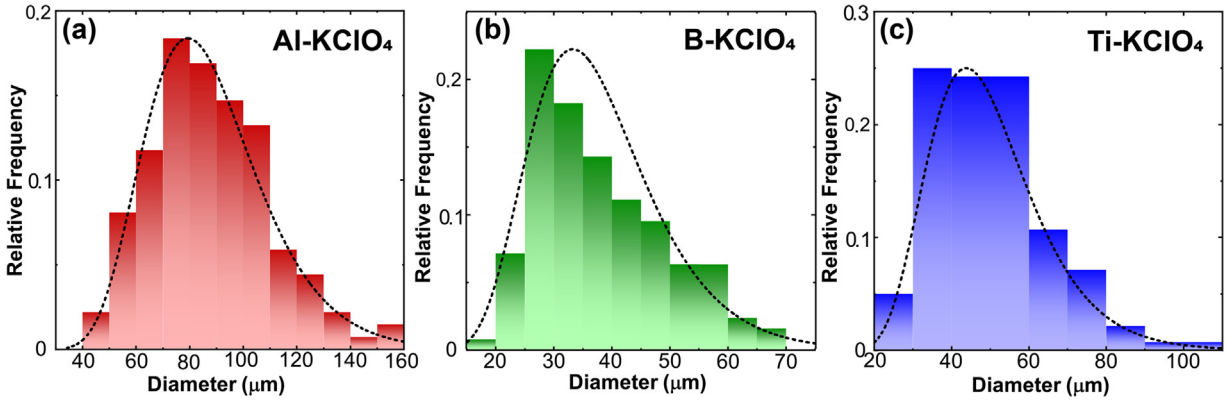

Fig. 2. Size distribution of agglomerates for Al-$KClO_4$ (a), B-$KClO_4$ (b) and Ti-$KClO_4$ (c). Note: only agglomerates that are about to depart from the burning surface or already departed. For B-$KClO_4$ and Ti-$KClO_4$, area equivalent diameter is displayed.

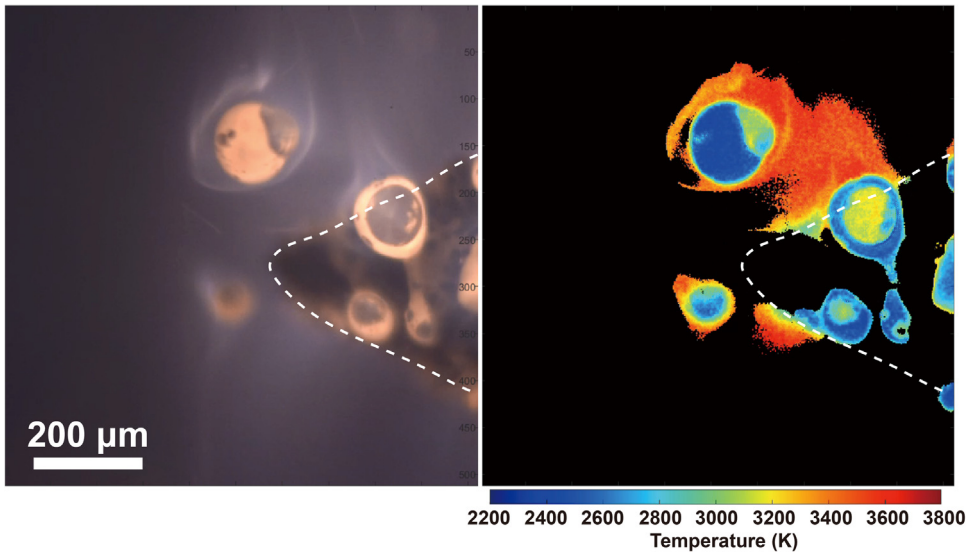

Fig. 3. Temperature map (right) from three-color (RGB) pyrometry for an image (left) from high-speed microscopy video of Al-$KClO_4$. High error points and low-intensity points were excluded from the calculation. The dashed line represents the boundary of the burning surface.

Table 1
Melting and boiling point of Al, Al_2O_3, B, B_2O_3, Ti, TiO_2, Ti_2O_3 with references, and measured temperature of burning agglomerates.

	Melting point (K)	Boiling point (K)	References		Measured temperature of burning agglomerates (K)
Al	930	2743	[22]	Al-$KClO_4$	2500
Al_2O_3	2345	3240	[22]		
B	2349	4200	[53]	B-$KClO_4$	1950
B_2O_3	723	2130	[53]		
Ti	1941	3560	[54]		
TiO_2	2116	3245	[39]	Ti-$KClO_4$	2350
Ti_2O_3	2400	3300	[39]		

as shown in Fig. S9) [40–42]. Figure 3 displays the demosaiced image and the temperature map for the Al-$KClO_4$ composite. As mentioned above, molten droplets are composed of aluminum as the main body and aluminum oxide as the cap. The estimated temperature for the Al body of the droplets around 2500 K is higher than the melting point at 930 K while lower than the boiling point of Al at 2743 K (Table 1). The estimated oxide cap temperature at ~3100 K is higher than the Al body temperature as well as the melting point of Al_2O_3 (Table 1). Chen et al. has seen similar observations where the oxide caps were hotter than Al bodies in molten droplets [22]. One may suppose that the difference in the measured temperature of the Al body and Al_2O_3 cap arises from the difference in their emissivity. Indeed, Al and Al_2O_3 have drastically different emissivity at high temperatures [35]. However, since we determine temperature based on the gray body emission assumption (emissivity remains constant when wavelength changes), the absolute value of emissivity cancels out [32].

Molten Al droplets are known to burn with vapor-phase combustion with the formation of a detached and diffusion-flame envelope away from the surface of the droplets where Al vaporizes, as shown in Fig. 3 [35,43]. Under vapor-phase combustion, nanometric smoke formed via homogeneous nucleation primarily consists of Al_2O_3 [35]. SEM/EDS images for post-combustion product confirm the presence of nanoparticles of Al_2O_3 (~100 nm, Fig. S11) along with the aluminum oxide microparticles as the final product (Fig. 7).

The temperature of these nanoparticles, which presumably represents the surrounding gas temperature due to their small size, is estimated to be ~3500 K, which is close to the adiabatic flame temperature of Al-$KClO_4$ at 3800 K as calculated with CHEETAH.

Boron has a characteristic green flame emission (between 450 and 600 nm) from BO_2 as an intermediate during combustion [38,44,45]. This emission (since it is non-graybody) can significantly affect the green-color channel, and lead to inaccuracy in temperature estimation from three-color (RGB) pyrometry, un-

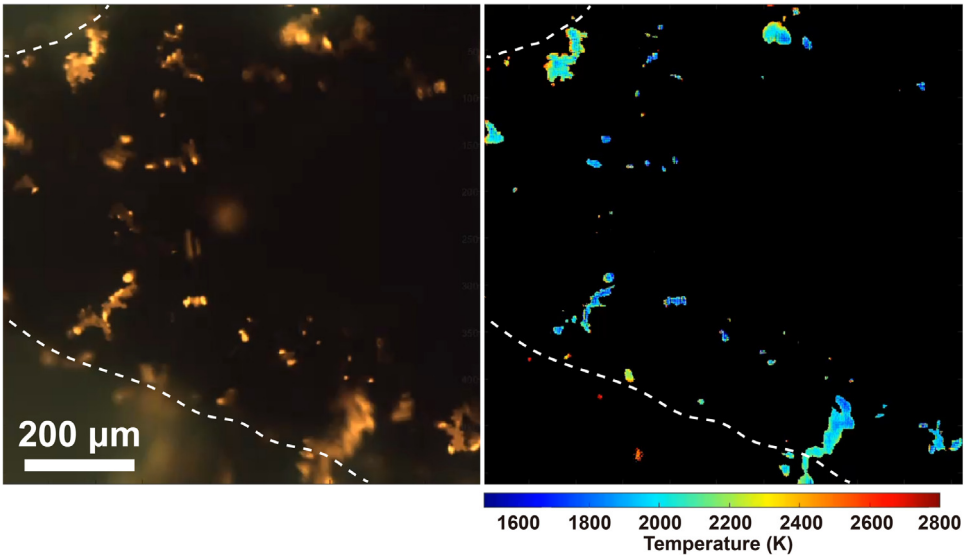

Fig. 4. Temperature map (right) from two-color (RB) pyrometry for an image (left) from high-speed microscopy video of B-$KClO_4$. High error points and low-intensity points were excluded from the calculation. The dashed lines represent boundaries of the burning surface.

der the gray-body assumption. To circumvent this problem, two-color (BR) pyrometry was employed (details can be found in Section 2.6) and the resultant temperature map is displayed in Fig. 4, which shows the burning particles are at ~1950 K. Fig. S10 shows temperature of the burning particles of B-$KClO_4$ measured with three-color (RGB) pyrometry is ~2250 K, which suggests a 300 K discrepancy caused by the molecular emission from BO_2.

It is generally accepted that the combustion of boron particles has two stages, the first stage is the burning of boron particles coated with a liquid B_2O_3 layer, and the second stage is combustion of bare boron after the removal of B_2O_3 [16,17,46,47]. The estimated temperature for agglomerates on the burning surface of B-$KClO_4$ is ~1950 K with two-color pyrometry, it is slightly lower than the boiling point of B_2O_3 (2130 K), therefore we conclude that the B_2O_3 is not completely removed and the combustion of agglomerates we observe is in the first stage boron combustion. Also, the estimated temperature is lower than the melting point of boron at 2349 K, shape of which is consistent with the observation that the particles are still agglomerates.

Ti-$KClO_4$ presents a more complex situation than B-$KClO_4$. The obtained temperature from three-color pyrometry for agglomerates on the Ti-$KClO_4$ burning surface is ~2350 K (Fig. 5), which is higher than the melting point of both Ti and TiO_2 (Table 1). The non-spherical shape of the agglomerates suggests the presence of other oxides with a higher melting point. Previous studies on titanium particle oxidation demonstrate that the oxidation process consists of different 'stages', one of which is the building-up of Ti_2O_3 beneath the TiO_2 outer surface [39,48]. Ti_2O_3 with a melting point of 2400 K, forms at a temperature of 2023 K, and the estimated temperature for agglomerates lies between these two temperatures [25,39]. Thus it is likely the agglomerates on the burning surface are mostly composed of Ti, Ti_2O_3, and TiO_2, with Ti_2O_3 being dominant in contributing to the shape, although other oxides including TiO and Ti_3O_5 may also be present [39]. Fragmentation, probably caused by the release of gas within the particle from the composition phase change, is an important characteristic during the combustion of Ti particles [24,25,49,50]. A previous study observed that the minimum particle size below which Ti particles no longer fragments is ~30 μm [49]. Minimal fragmentation is observed during Ti-$KClO_4$ composite burning, probably because the size of the agglomerates (at least in one dimension) is generally below the minimum particle size of ~30 μm for fragmentation [39,49].

3.3. Combustion performance

Al is known to combust in the vapor phase [34] while B and Ti in the condensed-phase [16,17,55], which implies that the combustion rate of Al should be significantly higher than B and Ti, whose combustion is limited by O_2 diffusion in the condensed-phase. However, we observe only moderate differences, as the burn rate of Al-$KClO_4$ (~10 cm/s) is about 4 times of B-$KClO_4$ (~2.5 cm/s) and about 2 times of Ti-$KClO_4$ (~5 cm/s), as shown in Fig. 6(b), and the resultant energy release rate of Al-$KClO_4$ is not dramatically higher than B-$KClO_4$ and Ti-$KClO_4$ (Fig. S12). A primary question now arises: why does Al-$KClO_4$ burns only moderately faster than B-$KClO_4$ and Ti-$KClO_4$?

Combustion of Al droplets is limited by the availability of Al vapor that depends on the evaporation rate of Al, therefore the combustion rate of Al decreases dramatically when droplet size increases since the evaporation rate of Al is significantly reduced due to the decreased overall surface/volume ratio. Typically this scaling is: Burn rate ~ $1/D^2$. The average size of Al droplets (~ 90 μm, Fig. 6(b)) is significantly larger than the starting Al nanoparticle (~100 nm, Fig. S1). The correlations between burn-times and sizes (Fig. 6(c)) of Al droplets and Ti particles (agglomerates) have been theoretically evaluated through application of a droplet evaporation model [34] and kinetic shrinking core model [55] (surface reaction controlled), respectively (details can be found in Section S5). A similar evaluation is not conducted for B particle combustion due to the lack of data and a well-accepted oxidation mechanism. These correlations suggest that although the calculated burn time of a 100 nm Al particle should be 4 orders of magnitude smaller than a 100 nm Ti particle (initial particles are both about 100 nm, as displayed in Fig. S1), the calculated burn time of a 100 μm Al droplet (~0.05 s) is only slightly lower than the burn time of a 50 μm Ti particle (~0.1 s), as shown in Fig. 6(c). This means the experimentally observed Al droplets burn only moderately faster than the Ti particles, since the size of Al droplets is large.

Visualization under microscopic conditions as seen in Fig. 6(a) shows that particles are not immediately ejected from the surface but ignite and subsequently burn for some time. A series of

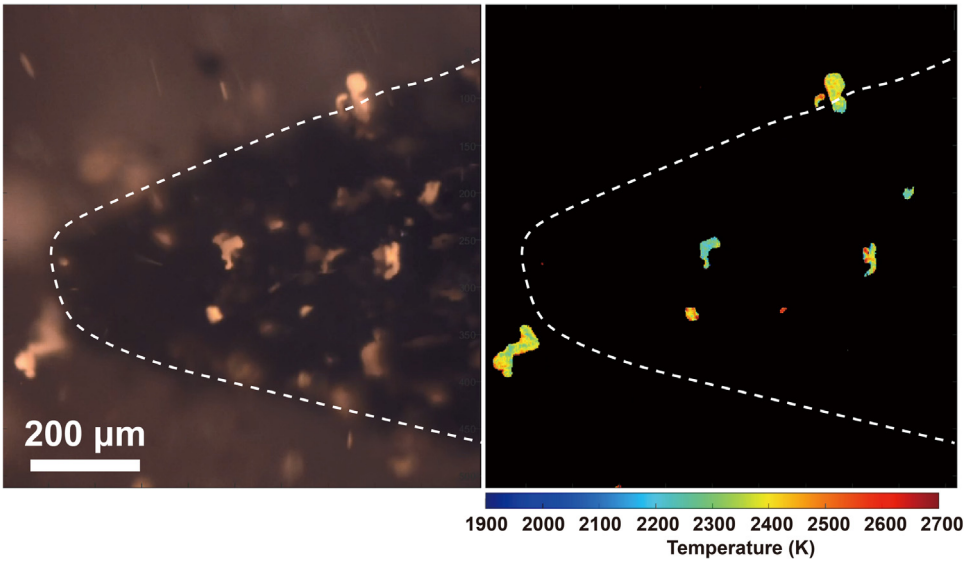

Fig. 5. Temperature map (right) from three-color (RGB) pyrometry for an image (left) from high-speed microscopy video of Ti-$KClO_4$. High error points and low-intensity points were excluded from the calculation. The dashed line represents boundary of the burning surface.

snapshots of a representative droplet/agglomerate forming, growing, and departing from the burning surface for Al, B, and Ti are displayed in Fig. 6(a), and the extracted surface residence times are estimated based on the time from the emergence of the droplets/agglomerates to their departure, and are tabulated in Fig. 6(d). It is noteworthy that the theoretical burn times of Al droplets and Ti particles are both much larger than their corresponding residence times on the burning surface, suggesting both Al droplets and Ti particles should have incomplete combustion before departing from the burning surface (Video S4). This is consistent with the experimental observation that the burning droplet/agglomerate continues burning after departure. As Al droplets and Ti agglomerates have similar temperatures (2500 K vs 2350 K), a higher surface residence time should result in more heat feedback to the unburnt solid composite that leads to a higher burn rate [58]. This also contributes to the observed higher burn rate of Al than Ti in addition to the aforementioned lower burn time of Al droplets compared to Ti particles.

It is clear from the images that luminous zones are indicative of significant burning away from the surface, the sharp edges of which terminate immediately near the burning surfaces (~0 mm, ~0.02 mm, and ~0.03 mm for Al-$KClO_4$, B-$KClO_4$, and Ti-$KClO_4$, respectively). Droplet/agglomerate velocity after departing from the burning surface is measured by tracking the location and the corresponding time. The result of this analysis is displayed in Fig. 6(e), which shows there is no significant droplet/agglomerate velocity difference between Al-$KClO_4$ and Ti-$KClO_4$. The expected burning distances of the dispersed Al droplets and Ti agglomerates are shown in Fig. 6(e) and are estimated based on their velocities and calculated burn times after departing from the burn surface (Fig. 6(d)). The result shows that the Al droplet would need to travel ~11 mm and Ti agglomerate ~16 mm for complete oxidation. These distances are significantly longer than the sharp edge of the luminous zone. This implies that the luminous zone cannot represent the complete flame zone.

3.4. Post combustion products

Further insight can be gained when microimaging observations are analyzed in tandem with SEM images of post-combustion products of these composites (Figs. 7 and S11). Micron-sized particles from Al-$KClO_4$ and B-$KClO_4$ are mostly spherical and fractal-shaped, respectively, consistent with morphology of the burning particles observed in microimaging (Figs. 1(a) and (b), 7(a) and (b)). However, different from the dominating fractal-shaped burning particles observed in microimaging, particles of post-combustion products from Ti-$KClO_4$ are spherical (Fig. 7(c)). This morphology change is attributed to the aforementioned transition of Ti_2O_3 to TiO_2 during oxidation after agglomerates depart from the burning surface.

SEM/EDS images of the sub-micron particles of post-combustion products of Al/B/Ti-$KClO_4$ composites also demonstrate the difference and similarity in combustion behaviors. As shown in Figure S11, KCl nanoparticles are produced for all three systems, from the condensation of KCl vapor as the product of decomposition of $KClO_4$. Both Al and B systems show significant aluminum oxide and boron oxide nanoparticles, respectively, but oxide nanoparticles are barely observed for the Ti system. The presence of aluminum oxide nanoparticles confirms the vapor phase reaction of Al. Boron oxide nanoparticles arise from the condensation of evaporated boron oxide as the measured temperature of the burning particles is close to the boiling point of B_2O_3 (Table 1). For Ti, both vapor phase combustion and oxide evaporation are negligible as the temperature is not sufficiently high. Unlike boron agglomerates being at the temperature close to the boiling point of B_2O_3 (difference is ~180 K), temperature of titanium agglomerates is much lower (~1000 K) than the boiling point of titanium oxides (TiO_2 and Ti_2O_3), therefore evaporated titanium oxides are less significant (Table 1).

3.5. Discussion on combustion characteristics

The combustion process of the three composites are summarized and represented in the illustration shown in Fig. 8. $KClO_4$ melts and decomposes concurrently at 610 °C, and the decomposition product KCl has a boiling point of 1412 °C [27,28], therefore presumably no $KClO_4$ or KCl is present in solid state during burning. The combustion behavior differences between Al-$KClO_4$ and B-$KClO_4$ or Ti-$KClO_4$ as well as the similarity between B-$KClO_4$ and Ti-$KClO_4$ are attributed to the physical property (e.g. melting and boiling point) of their corresponding metal and metal oxide, as shown in Table 1. Although the Al_2O_3 shell has a relatively high melting point, the phase transition from amorphous to γ-Al_2O_3 below 900 K introduces voids in the oxide shell, enabling

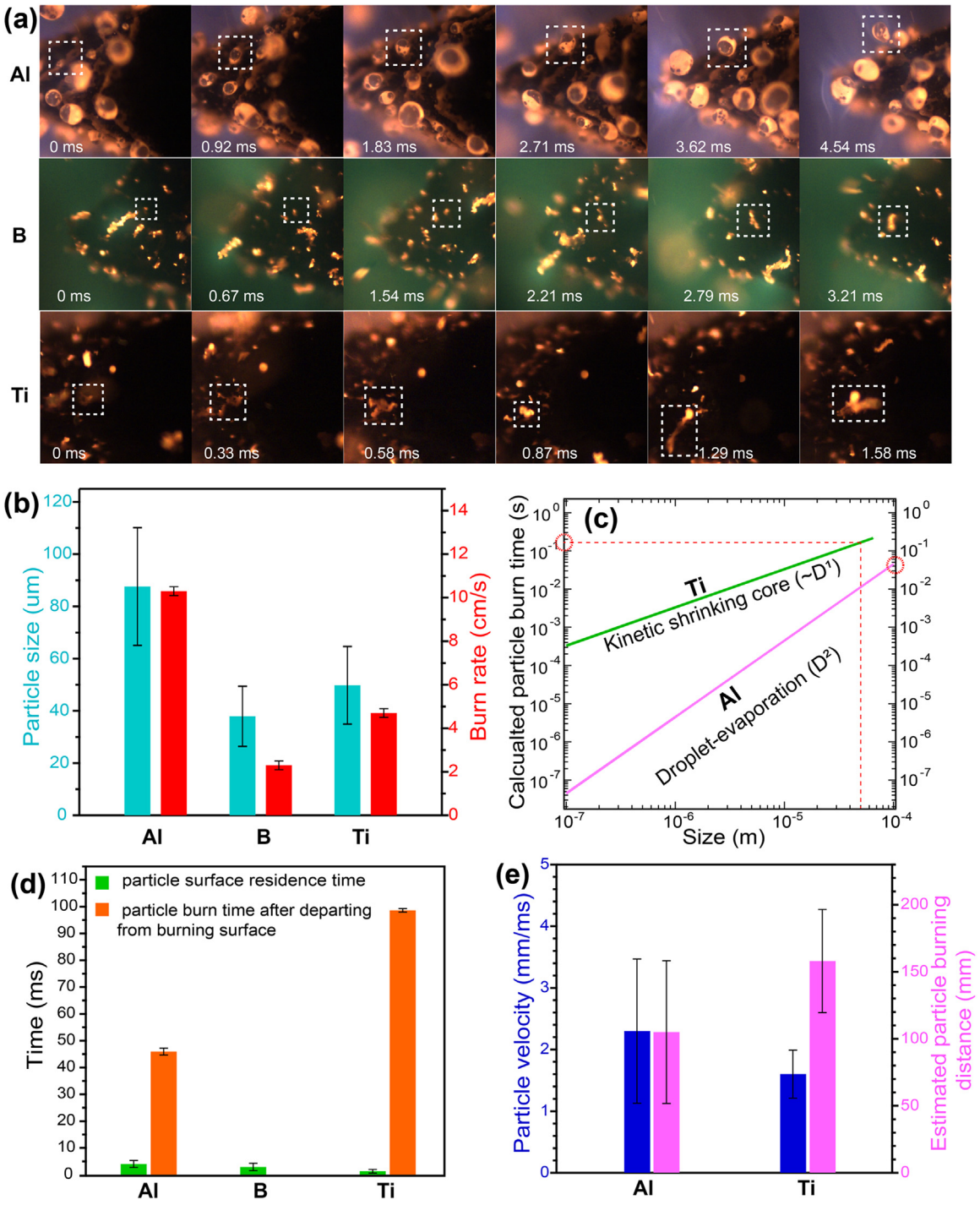

Fig. 6. Time-resolved snapshots of the particles (droplets/agglomerates) evolving before departing from burning surface (a), particle size and burn rate of different composites (b), correlations between burn-times and sizes of Al droplet and Ti agglomerate based on droplet-evaporation model and kinetic shrinking core model, respectively (c), particle surface residence time on the burning surface and particle burn time of the observed size (100 μm for Al and 50 μm for Ti) after departing from the burning surface (d), and measured particle velocity and estimated particle burning distance for complete oxidation (e).

the molten Al core to leak through the oxide shell when the temperature reaches its melting point at 930 K [51]. As oxidation of Al continues, and sintering/coalescence occurs below the melting point of Al_2O_3 because the high mobility of Al within Al_2O_3 likely softens it [52]. Molten Al on the surface merge to form larger droplets before they depart the surface. Based on analysis of the images this process takes on the order of ~ 4 ms.

B and Ti have much higher melting points compared to Al, and thus are relatively less mobile with considerably smaller atomic diffusivities. This explains why B and Ti primarily form fractal-like structures rather than spherical droplets (Fig. 8). As mentioned in Section 3.1, some of these fractal-shaped agglomerates may ball up into spheres during burning, and agglomerates of Ti-$KClO_4$ have a higher tendency for becoming spheres than those of B-$KClO_4$. The measured temperature of agglomerates on B-$KClO_4$ burning surface is ~400 K lower than the melting point of B, thus it is less likely for the agglomerates to melt and become spheres without a temperature increase. As for Ti-$KClO_4$, the fractal-shaped agglomerates

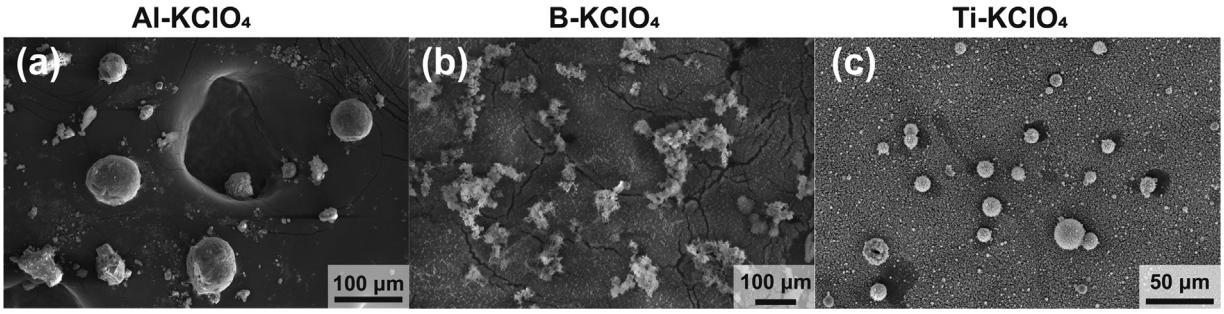

Fig. 7. SEM images of microparticles for post-combustion products of Al-$KClO_4$ (a), B-$KClO_4$ (b), and Ti-$KClO_4$ (c). Note: For Al-$KClO_4$, the product was water-washed briefly to remove KCl so that large agglomerates can stay on the carbon tap for SEM. More details can be found in Section 2.3.

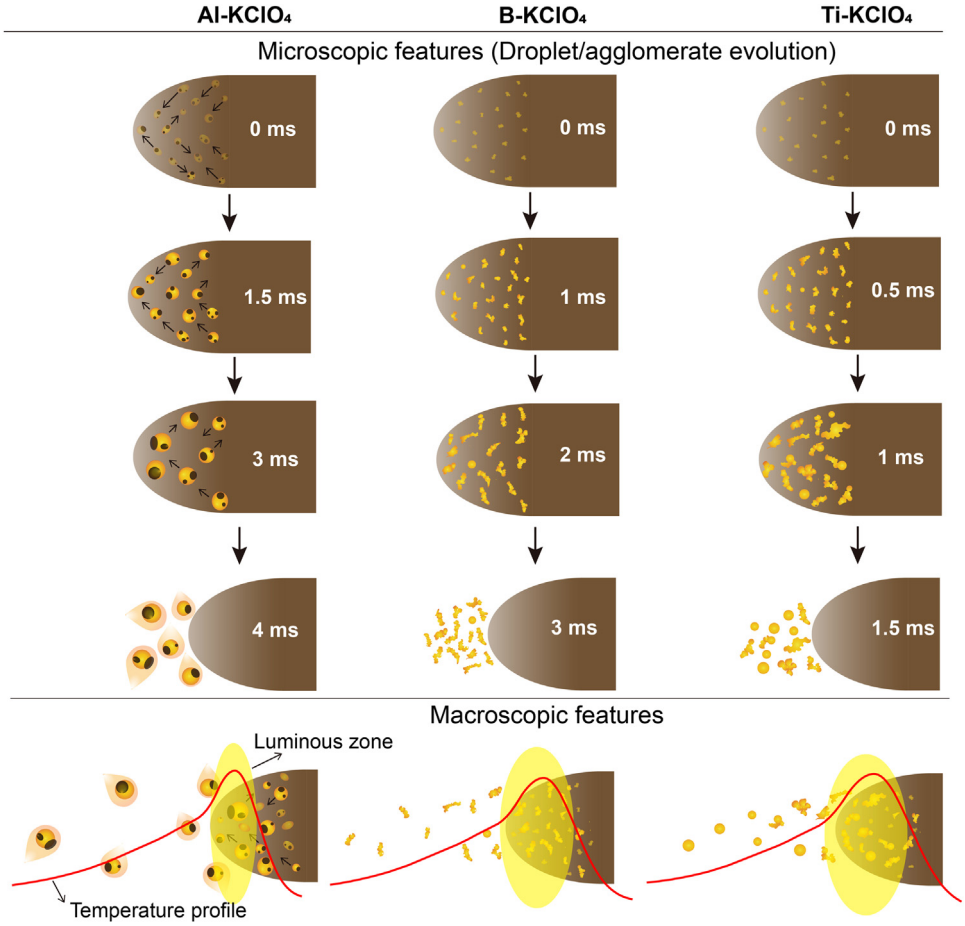

Fig. 8. Illustration of the microscopic features (droplet/agglomerate evolution) with corresponding time stamps as well as the macroscopic features of Al-$KClO_4$ (left) and B-$KClO_4$ (middle) and Ti-$KClO_4$ (right).

are in the combustion stage where Ti_2O_3 dominates the structure. As agglomerates continue burning, the amount of TiO_2 increases while Ti_2O_3 and other lower oxides diminish. The newly-formed TiO_2 melts upon formation, which means that the agglomerates transition into spheres even if the temperature remains invariant. There is minimal temperature change observed along the burning of agglomerates on the burning surface of both B-$KClO_4$ and Ti-$KClO_4$, explaining why agglomerates of Ti-$KClO_4$ are more likely to become spheres than those of B-$KClO_4$. The time spans from emergence to departure of B and Ti agglomerates are ~3 ms and ~ 1.5 ms, respectively, both are slightly lower than the Al droplets, contributing to lower heat feedback to the composite and thus lower burn rates, as discussed in Section 3.3.

Macroscopic combustion features of the three composites are also displayed in Fig. 8. As discussed in Section 3.3, the luminous zone ends immediately after the burning surface although the droplets/agglomerates are not completely combusted in that region, indicating a temperature drop downstream.

4. Conclusions

In this paper, we study the combustion characteristics of high-loading Al-$KClO_4$, B-$KClO_4$, and Ti-$KClO_4$ composites with high-speed microscopy and pyrometry and find that combustion characteristics of these composites are strongly dependent on the fuel type. Mobile Al droplets with Al_2O_3 caps form on the burning surface of Al-$KClO_4$, then coalesce into larger droplets before departing from the burning surface. As for B-$KClO_4$ and Ti-$KClO_4$, fractal-shaped agglomerates form. Temperatures of the burning particles are determined with color imaging-pyrometry. The combustion be-

havior difference between Al-$KClO_4$ and B/Ti-$KClO_4$ as well as the similarity between B-$KClO_4$ and Ti-$KClO_4$ are attributed to the physical properties, e.g. melting and boiling points, of these fuels and their corresponding oxides. Particles reside and burn on the propellant surface with the residence time on the order of ∼1–5 ms. This is significantly lower than the theoretical particle burn time, implying incomplete particle combustion on the burning surface. This is consistent with the experimental observation that particles continue to burn after departing the burning surface. The estimated particle downstream burning distance is drastically larger than the observed luminous zone, suggesting the luminous zone does not represent the complete flame zone. Since Al combusts in the vapor phase while B and Ti combust in the condense phase, the burn rate of Al should be significantly higher than B and Ti, However, the differences are not as drastic as expected because the formation of much larger droplets of Al results in dramatically longer particle burn times.

Declaration of Competing Interest

On behalf of all the authors, we declare no conflict of interest. This work is original and has not been considered for publication elsewhere.

Acknowledgments

This work was supported by the ONR and the MSEE DTRA University Research Alliance.

Supplementary materials

Supplementary material associated with this article can be found, in the online version, at doi:10.1016/j.combustflame.2023.112747.

References

[1] H. Wang, D.J. Kline, M.R. Zachariah, In-operando high-speed microscopy and thermometry of reaction propagation and sintering in a nanocomposite, Nat. Commun. 10 (2019) 3032, doi:10.1038/s41467-019-10843-4.
[2] D.J. Shin, W.D. Kim, S. Lee, D.C. Lee, Nanothermite of Al nanoparticles and three-dimensionally ordered macroporous CuO: mechanistic insight into oxidation during thermite reaction, Combust. Flame. 189 (2018) 87–91, doi:10.1016/j.combustflame.2017.10.018.
[3] W. He, P.-J. Liu, G.-Q. He, M. Gozin, Q.-L. Yan, Highly reactive metastable intermixed composites (MICs): preparation and characterization, Adv. Mater. 30 (2018) 1706293, doi:10.1002/adma.201706293.
[4] V. Baijot, D.-R. Mehdi, C. Rossi, A. Estève, A multi-phase micro-kinetic model for simulating aluminum based thermite reactions, Combust. Flame. 180 (2017) 10–19, doi:10.1016/j.combustflame.2017.02.031.
[5] Y.-C. Chiang, M.-H. Wu, Assembly and reaction characterization of a novel thermite consisting aluminum nanoparticles and CuO nanowires, Proc. Combust. Inst. 36 (2017) 4201–4208, doi:10.1016/j.proci.2016.06.176.
[6] K.T. Sullivan, J.D. Kuntz, A.E. Gash, The role of fuel particle size on flame propagation velocity in thermites with a nanoscale oxidizer, Propellants Explos. Pyrotech. 39 (2014) 407–415, doi:10.1002/prep.201400020.
[7] N. Zohari, M.H. Keshavarz, S.A. Seyedsadjadi, The advantages and shortcomings of using nano-sized energetic materials, Cent. Eur. J. Energ. Mater. 10 (2013) http://yadda.icm.edu.pl/baztech/element/bwmeta1.element.baztech-3e0dd85e-6d8e-465b-a1a3-11263f846ff2. (Accessed June 2, 2021).
[8] K.T. Sullivan, N.W. Piekiel, C. Wu, S. Chowdhury, S.T. Kelly, T.C. Hufnagel, K. Fezzaa, M.R. Zachariah, Reactive sintering: an important component in the combustion of nanocomposite thermites, Combust. Flame. 159 (2012) 2–15, doi:10.1016/j.combustflame.2011.07.015.
[9] G.C. Egan, K.T. Sullivan, T.Y. Olson, T.Y.-J. Han, M.A. Worsley, M.R. Zachariah, Ignition and combustion characteristics of nanoaluminum with copper oxide nanoparticles of differing oxidation state, J. Phys. Chem. C. 120 (2016) 29023–29029, doi:10.1021/acs.jpcc.6b11081.
[10] S.K. Valluri, M. Schoenitz, E. Dreizin, Bismuth fluoride-coated boron powders as enhanced fuels, Combust. Flame. 221 (2020) 1–10, doi:10.1016/j.combustflame.2020.07.023.
[11] M.C. Rehwoldt, Y. Yang, H. Wang, S. Holdren, M.R. Zachariah, Ignition of nanoscale titanium/potassium perchlorate pyrotechnic powder: reaction mechanism study, J. Phys. Chem. C. 122 (2018) 10792–10800, doi:10.1021/acs.jpcc.8b03164.
[12] T.R. Sippel, S.F. Son, L.J. Groven, Aluminum agglomeration reduction in a composite propellant using tailored Al/PTFE particles, Combust. Flame. 161 (2014) 311–321, doi:10.1016/j.combustflame.2013.08.009.
[13] G. Young, H. Wang, M.R. Zachariah, Application of nano-aluminum/nitrocellulose mesoparticles in composite solid rocket propellants, Propellants Explos. Pyrotech. 40 (2015) 413–418, doi:10.1002/prep.201500020.
[14] L. Meda, G. Marra, L. Galfetti, F. Severini, L. De Luca, Nano-aluminum as energetic material for rocket propellants, Mater. Sci. Eng. C. 27 (2007) 1393–1396, doi:10.1016/j.msec.2006.09.030.
[15] H. Wang, J.B. DeLisio, G. Jian, W. Zhou, M.R. Zachariah, Electrospray formation and combustion characteristics of iodine-containing Al/CuO nanothermite microparticles, Combust. Flame. 162 (2015) 2823–2829, doi:10.1016/j.combustflame.2015.04.005.
[16] C.L. Yeh, K.K. Kuo, Ignition and combustion of boron particles, Prog. Energy Combust. Sci. 22 (1996) 511–541, doi:10.1016/S0360-1285(96)00012-3.
[17] A. Ulas, K.K. Kuo, C. Gotzmer, Ignition and combustion of boron particles in fluorine-containing environments, Combust. Flame. 127 (2001) 1935–1957, doi:10.1016/S0010-2180(01)00299-1.
[18] Study of titanium potassium perchlorate combustion using electric field holography and imaging pyrometry | AIAA SCITECH 2022 Forum, AIAA SciTech Forum. (n.d.). https://arc.aiaa.org/doi/abs/10.2514/6.2022-1522 (Accessed January 3, 2022).
[19] J.C. Melcher, H. Krier, R.L. Burton, Burning aluminum particles inside a laboratory-scale solid rocket motor, J. Propuls. Power. 18 (2002) 631–640, doi:10.2514/2.5977.
[20] E.L. Dreizin, Experimental study of stages in aluminium particle combustion in air, Combust. Flame. 105 (1996) 541–556, doi:10.1016/0010-2180(95)00224-3.
[21] V.V. Karasev, A.A. Onischuk, O.G. Glotov, A.M. Baklanov, A.G. Maryasov, V.E. Zarko, V.N. Panfilov, A.I. Levykin, K.K. Sabelfeld, Formation of charged aggregates of Al2O3 nanoparticles by combustion of aluminum droplets in air, Combust. Flame. 138 (2004) 40–54, doi:10.1016/j.combustflame.2004.04.001.
[22] Y. Chen, D.R. Guildenbecher, K.N.G. Hoffmeister, M.A. Cooper, H.L. Stauffacher, M.S. Oliver, E.B. Washburn, Study of aluminum particle combustion in solid propellant plumes using digital in-line holography and imaging pyrometry, Combust. Flame. 182 (2017) 225–237, doi:10.1016/j.combustflame.2017.04.016.
[23] A.W. Marsh, G.T. Wang, J.D. Heyborne, D.R. Guildenbecher, Y.C. Mazumdar, Time-resolved size, velocity, and temperature statistics of aluminum combustion in solid rocket propellants, Proc. Combust. Inst. 38 (2021) 4417–4424, doi:10.1016/j.proci.2020.08.010.
[24] E. Shafirovich, S.K. Teoh, A. Varma, Combustion of levitated titanium particles in air, Combust. Flame. 152 (2008) 262–271, doi:10.1016/j.combustflame.2007.05.008.
[25] I.E. Molodetsky, E.P. Vicenzi, E.L. Dreizin, C.K. Law, Phases of titanium combustion in air, Combust. Flame. 112 (1998) 522–532, doi:10.1016/S0010-2180(97)00146-6.
[26] D. Liu, Z. Xia, L. Huang, J. Hu, Boron particle combustion in solid rocket ramjets, J. Aerosp. Eng. 28 (2015) 04014112, doi:10.1061/(ASCE)AS.1943-5525.0000443.
[27] Y. Wang, H. Wang, F. Xu, P. Ghildiyal, M.R. Zachariah, Effect of alkali metal perchlorate and iodate type on boron ignition: the role of oxidizer phase change, Chem. Eng. J. 446 (2022) 136786, doi:10.1016/j.cej.2022.136786.
[28] X. Xu, X. Wang, P. Li, Y. Li, Q. Hao, B. Xiao, H. Elsentriecy, D. Gervasio, Experimental test of properties of KCl–MgCl2 eutectic molten salt for heat transfer and thermal storage fluid in concentrated solar power systems, J. Sol. Energy Eng. 140 (2018), doi:10.1115/1.4040065.
[29] H. Wang, J. Shen, D.J. Kline, N. Eckman, N.R. Agrawal, T. Wu, P. Wang, M.R. Zachariah, Direct writing of a 90 wt% particle loading nanothermite, Adv. Mater. 31 (2019) 1806575, doi:10.1002/adma.201806575.
[30] H. Wang, B. Julien, D. Kline, Z. Alibay, M. Rehwoldt, C. Rossi, M. Zachariah, Probing the reaction zone of nanolaminates at ∼μs time and ∼μm spatial resolution, J. Phys. Chem. C. 124 (2020) 13679–13687, doi:10.1021/acs.jpcc.0c01647.
[31] D.J. Kline, Z. Alibay, M.C. Rehwoldt, A. Idrogo-Lam, S.G. Hamilton, P. Biswas, F. Xu, M.R. Zachariah, Experimental observation of the heat transfer mechanisms that drive propagation in additively manufactured energetic materials, Combust. Flame. 215 (2020) 417–424, doi:10.1016/j.combustflame.2020.01.020.
[32] R.J. Jacob, D.J. Kline, M.R. Zachariah, High speed 2-dimensional temperature measurements of nanothermite composites: probing thermal vs. gas generation effects, J. Appl. Phys. 123 (2018) 115902, doi:10.1063/1.5021890.
[33] H. Wang, D.J. Kline, M.C. Rehwoldt, M.R. Zachariah, Carbon fibers enhance the propagation of high loading nanothermites: in situ observation of microscopic combustion, ACS Appl. Mater. Interfaces. (2021), doi:10.1021/acsami.1c02911.
[34] V.N. Emelyanov, I.V. Teterina, K.N. Volkov, Dynamics and combustion of single aluminium agglomerate in solid propellant environment, Acta Astronaut. 176 (2020) 682–694, doi:10.1016/j.actaastro.2020.03.046.
[35] J. Harrison, M.Q. Brewster, Analysis of thermal radiation from burning aluminum in solid propellants, Combust. Theory Model. 13 (2009) 389–411, doi:10.1080/13647830802684318.
[36] E.L. Dreizin, Experimental study of aluminum particle flame evolution in normal and micro-gravity, Combust. Flame. 116 (1999) 323–333, doi:10.1016/S0010-2180(97)00331-3.

[37] M. Spalding, H. Krier, R. Burton, M. Spalding, H. Krier, R. Burton, Emission spectroscopy during ignition of boron particles at high pressure, in: 35th Aerosp, Sci. Meet. Exhib., American Institute of Aeronautics and Astronautics (1997) https://doi.org/10.2514/6.1997-119.
[38] M.J. Spalding, H. Krier, R.L. Burton, Boron suboxides measured during ignition and combustion of boron in shocked Ar/F/O_2 and Ar/N_2/O_2 mixtures, Combust. Flame. 120 (2000) 200–210, doi:10.1016/S0010-2180(99)00082-6.
[39] O.G. Glotov, Ignition and combustion of titanium particles: experimental methods and results, Phys.-Uspekhi 62 (2019) 131, doi:10.3367/UFNe.2018.04.038349.
[40] P. Biswas, G.W. Mulholland, M.C. Rehwoldt, D.J. Kline, M.R. Zachariah, Microwave absorption by small dielectric and semi-conductor coated metal particles, J. Quant. Spectrosc. Radiat. Transf. 247 (2020) 106938, doi:10.1016/j.jqsrt.2020.106938.
[41] P. Biswas, P. Ghildiyal, G.W. Mulholland, M.R. Zachariah, Modelling and simulation of field directed linear assembly of aerosol particles, J. Colloid Interface Sci. 592 (2021) 195–204, doi:10.1016/j.jcis.2021.02.050.
[42] C.F. Bohren, D.R. Huffman, Absorption and Scattering of Light by Small Particles, John Wiley & Sons, 2008.
[43] M.W. Beckstead, A summary of aluminum combustion, Brigham Young Univ Provo Ut, 2004.
[44] D. Liang, J. Liu, J. Xiao, J. Xi, Y. Wang, Y. Zhang, J. Zhou, Energy release properties of amorphous boron and boron-based propellant primary combustion products, Acta Astronaut. 112 (2015) 182–191, doi:10.1016/j.actaastro.2015.03.019.
[45] J. Xi, J. Liu, Y. Wang, D. Liang, J. Zhou, Effect of metal hydrides on the burning characteristics of boron, Thermochim. Acta. 597 (2014) 58–64, doi:10.1016/j.tca.2014.10.017.
[46] S.C. Li, F.A. Williams, F. Takahashi, An investigation of combustion of boron suspensions, Symp. Int. Combust. 22 (1989) 1951–1960, doi:10.1016/S0082-0784(89)80210-3.
[47] G. Young, K. Sullivan, M.R. Zachariah, K. Yu, Combustion characteristics of boron nanoparticles, Combust. Flame. 156 (2009) 322–333, doi:10.1016/j.combustflame.2008.10.007.
[48] O. Kubaschewski, G.V. Samsonov (Eds.), The Oxide Handbook, IFI/Plenum, New York and London, 1982 463 Seiten, Preis: $75,-, Berichte Bunsenges. Für Phys. Chem. 86 (1982) 761–762, doi:10.1002/bbpc.19820860820.
[49] O.G. Glotov, Combustion of spherical agglomerates of titanium in air. II. Results of experiments, Combust. Explos. Shock Waves. 49 (2013) 307–319, doi:10.1134/S0010508213030076.
[50] C. Badiola, E.L. Dreizin, Combustion of micron-sized particles of titanium and zirconium, Proc. Combust. Inst. 34 (2013) 2237–2243, doi:10.1016/j.proci.2012.05.089.
[51] M.A. Trunov, M. Schoenitz, E.L. Dreizin, Effect of polymorphic phase transformations in alumina layer on ignition of aluminium particles, Combust. Theory Model. 10 (2006) 603–623, doi:10.1080/13647830600578506.
[52] P. Chakraborty, M.R. Zachariah, Do nanoenergetic particles remain nano-sized during combustion? Combust. Flame. 161 (2014) 1408–1416, doi:10.1016/j.combustflame.2013.10.017.
[53] S. Huang, S. Deng, Y. Jiang, X. Zheng, Experimental effective metal oxides to enhance boron combustion, Combust. Flame. 205 (2019) 278–285, doi:10.1016/j.combustflame.2019.04.018.
[54] W.M. Haynes, CRC Handbook of Chemistry and Physics, 95th ed., CRC Press, Hoboken, 2014 http://search.ebscohost.com/login.aspx?direct=true&scope=site&db=nlebk&db=nlabk&AN=1631986 (Accessed March 6, 2022).
[55] Y. Zong, R.J. Jacob, S. Li, M.R. Zachariah, Size resolved high temperature oxidation kinetics of nano-sized titanium and zirconium particles, J. Phys. Chem. A. 119 (2015) 6171–6178, doi:10.1021/acs.jpca.5b02590.
[56] K. McNesby, S. Dean, R. Benjamin, J. Grant, J. Anderson, J. Densmore, Imaging pyrometry for most color cameras using a triple pass filter, Rev. Sci. Instrum. 92 (2021), doi:10.1063/5.0037230.
[57] H. Wang, Y. Wang, M. Garg, J.S. Moore, M.R. Zachariah, Unzipping polymers significantly enhance energy flux of aluminized composites, Combust. Flame. 244 (2022) 112242, doi:10.1016/j.combustflame.2022.112242.
[58] , Survey of rocket propellants and their combustion characteristics, Fundam. Solid-Propellant Combust., American Institute of Aeronautics and Astronautics (1984), pp. 1–52, doi:10.2514/5.9781600865671.0001.0052.